NANO LETTERS
Letter
pubs.acs.org/NanoLett

First-Principles Theoretical Studies and Nanocalorimetry Experiments on Solid-State Alloying of Zr−B

Dongwoo Lee,[†] Joost J. Vlassak,[*,†] and Kejie Zhao[*,‡]

[†]School of Engineering and Applied Sciences, Harvard University, Cambridge, Massachusetts 02138, United States
[‡]School of Mechanical Engineering, Purdue University, West Lafayette, Indiana 47906, United States

Ⓢ *Supporting Information*

ABSTRACT: The thermodynamics and kinetics of the solid-state alloying of Zr−B, underlying a variety of synthesis processes of the ultrahigh-temperature ceramic ZrB_2, are widely unknown. We investigate the energetics, diffusion kinetics, and structural evolution of this system using first-principles computational methods. We identify the diffusion pathways in the interpenetrating network of interstitial sites for a single B atom and demonstrate a dominant rate-controlling step from the octahedral to the crowdion site that is distinct from the conventional mechanism of octahedral−tetrahedral transition in hexagonal close-packed structures. In the intermediate compounds ZrB_x, $0 < x \leq 2$, the diffusivity of B is highly dependent on the composition while reaching a minimum for ZrB. The activation barrier of diffusion in ZrB_2 is in good agreement with nanocalorimetry measurements performed on Zr/B reactive nanolaminates.

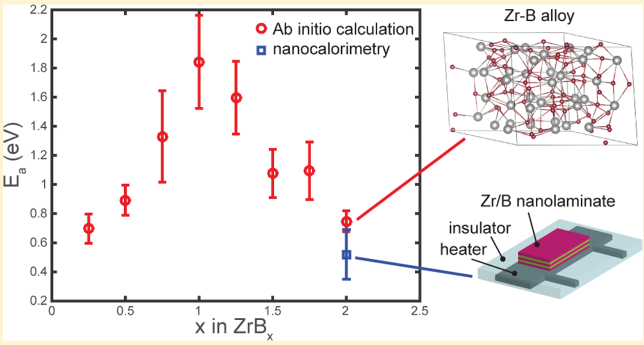

KEYWORDS: *Diffusion, ZrB_2, first-principles, nanocalorimetry*

Zirconium diboride (ZrB_2) exhibits a unique combination of properties including extremely high melting temperature, corrosion resistance, and mechanical hardness that make it an ideal structural material for extreme environments.[1−3] ZrB_2 is also a promising candidate in optoelectronic and microelectronic applications due to its excellent electrical and thermal conductivities, metal-like optical properties, and the similarity of in-plane lattice constants and thermal expansion coefficients between ZrB_2 and GaN.[4−8] Large scale processing of dense structures of ZrB_2 is, however, challenging, which makes implementation in practical systems difficult.

ZrB_2 is generally synthesized via reduction processes,[1] chemical routes,[7,9,10] or reactive processes.[11,12] Solid-state alloying of Zr−B is the intrinsic process underlying nearly all the fabrication routes. However, a fundamental understanding of the thermodynamics and kinetics in the intermediate compounds of zirconium boride is critically missing. Experimental measurements of the activation energy for Zr−B diffusion show a large variation of 0.47−1.99 eV.[12,13] A few related theoretical studies are available including research on point defects and self-diffusion of Zr,[14−16] structures and physical properties of ZrB_2,[17−20] and phase stability of Zr−B compounds.[21,22]

To reach a comprehensive understanding of the solid-state alloying process of Zr−B, we investigate the energetics and diffusion kinetics as well as the structural evolution with systematic variation of the B concentration in the Zr host. First-principles computational methods within the framework of density functional theory (DFT) are employed. We identify the diffusion pathways in the interpenetrating network of interstitial sites for a single B atom and demonstrate the anisotropic nature of B transport in Zr. The dominant hopping step is the hop from the octahedral to the crowdion site, which is distinct from the conventional mechanism of octahedral−tetrahedral transition in hexagonal close-packed (hcp) structures. In the intermediate compounds ZrB_x, $0 < x \leq 2$, the B diffusivity varies by a few orders of magnitude depending on the B concentration and the temperature of interest. It reaches a minimum for ZrB that originates from the lowest energy landscape at the rational stoichiometry of ZrB and from the drastic structural transition beyond this composition. We further perform nanocalorimetry measurements on Zr/B reactive nanolaminates to extract the kinetic parameters of the solid-state reaction. The diffusion barrier of ZrB_2 in atomistic modeling is in good agreement with the experimental values.

We first study the energetics of B insertion into the crystalline Zr host. We begin this investigation by determining the stable positions of a single B atom in α-Zr, which has a hcp structure with a space group of $P6_3/mmc$ and lattice parameters $a = b = 3.23$ Å, and $c = 5.17$ Å.[14,16] A single B atom is placed into a supercell at nonequivalent sites, shown in Figure 1a,

Received: June 8, 2015
Revised: August 13, 2015
Published: August 27, 2015

DOI: 10.1021/acs.nanolett.5b02260
Nano Lett. 2015, 15, 6553−6558

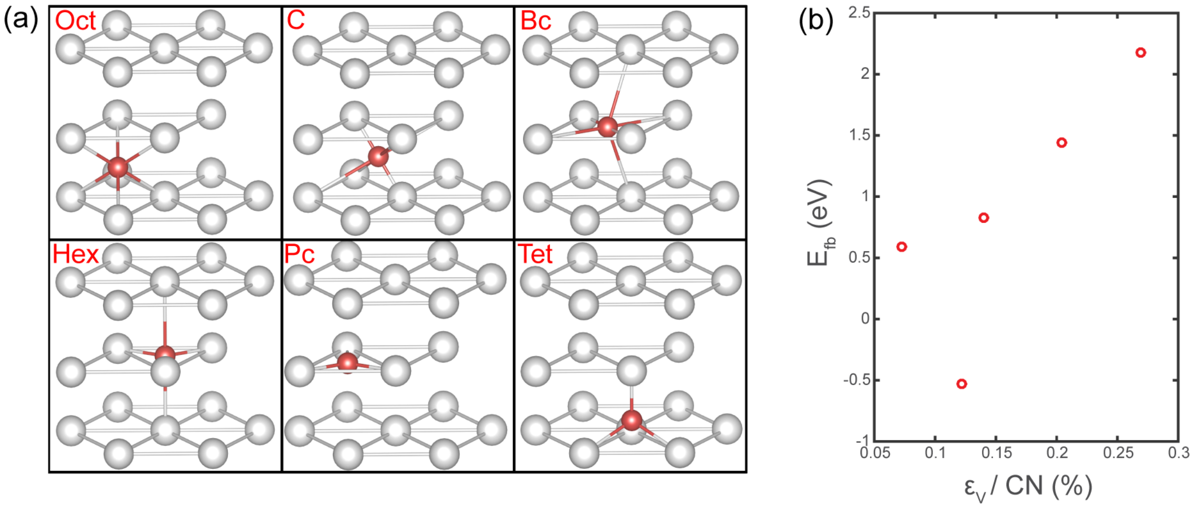

Figure 1. (a) Positions and local environments of the interstitial sites in Zr. (b) The formation energy of the interstitial B at each site versus volumetric strain/coordination number.

including the octahedral site (Oct), the crowdion site (C), the basal bond center (Bc), the hexagonal site (Hex), the plane center (Pc), the tetrahedral site (Tet), and the substitutional site. We calculate the formation energy to compare the thermodynamic stability of B at the various sites. We take the energies of a Zr atom (E_{Zr}) and a B atom (E_B) in bulk form as reference energies, with $E_{nB\text{-}Zr}$ being the total energy of the system containing nB atoms in a cell that contains $(54 - m)$ Zr atoms ($m = 0$, except when B is on the substitutional site, in which case $m = 1$). The formation energy per B atom $E_{fB}(n)$ is

$$E_{fB}(n) = [E_{nB-Zr} - (54 - m)E_{Zr} - nE_B]/n \tag{1}$$

Table 1 lists calculated formation energies at various sites and associated structural parameters, where ε_V is the volumetric strain and CN represents the coordination number, which is calculated by a cutoff of 10% elongation of the Zr−B bond in crystalline ZrB_2 ($P6/mmm$, a, b = 3.17 Å, c = 3.53 Å).[1] The formation energies at the different positions indicate that B insertion at the Oct site results in the only energetically favorable structure. The C, Bc, Hex, and Pc sites are defined as metastable positions because the B atom would be stabilized at the initial insertion site upon relaxation, but the formation energies show positive values. Interestingly, the Tet site is unstable in that a B atom placed at this site will slide to the nearby hexahedral site during relaxation. The Tet site has also been found unstable for O, N, and C impurities in hcp Ti.[23,24] As a reference, we also calculate the formation energy for substitutional B in Zr. The large formation energy indicates that substitution of Zr by B is energetically costly and may occur only at high temperatures. We note that B insertion at interstitial sites with lower formation energies results in relatively small volumetric strains (ε_V) and large coordination numbers representing a less repulsive and more cooperative local environment. This correlation is plotted in Figure 1b, which shows a nearly monotonic increase of E_{fB} as a function of ε_V /CN. The static energy barrier (ΔE_s) for B transport can be estimated by subtracting E_{fB} for each interstitial site from that of the most stable site (Oct). This procedure suggests a preferred diffusion path, Oct-C-Oct with ΔE_s = 1.12 eV, which occurs between the basal planes of the Zr lattice. The next favorable path is Oct-Bc-Oct with ΔE_s = 1.35 eV, which corresponds to diffusion along the c-axis.

Table 1. Structural and Energetic Features of a Single B Atom at Various Sites in the Zr Lattice

boron sites	position	E_{fB} (eV)	CN	ε_V (%)	stability
octahedral (Oct)	(0.33, 0.67, 0.25)	−0.53	6	0.732	stable
crowdion (C)	(0.83, 0.17, 0.25)	0.59	6	0.435	metastable
basal bond center (Bc)	(0.67, 0.83, 0.50)	0.82	6	0.840	metastable
hexahedral (Hex)	(0.00, 0.00, 0.50)	1.45	5	1.021	metastable
plane center (*Pc*)	(0.33, 0.67, 0.50)	2.18	3	0.807	metastable
tetrahedral (Tet)	(0.67, 0.33, 017)	2.03	4	1.134	unstable
substitutional (Sub)	(0, 0, 0)	1.86	12	−1.605	metastable

In order to determine the diffusion pathway of B, we calculate the activation energies along various diffusion trajectories using the nudged elastic band (NEB) method. In the NEB calculations, all atoms in the initial and final states are first relaxed in a supercell with fixed volume and shape. We then sample the diffusion pathway consisting of three intermediate configurations. The NEB path is constructed by linear interpolation of the atomic coordinates. Then, the path is relaxed until the force on each atom is smaller than 0.02 eV/ Å. The activation energy versus the reaction coordinate is illustrated in Figure 2 for several diffusion paths. Table 2 lists the calculated energy barrier (ΔE_{NEB}) and the energy corresponding to the occupancy probability of B at the initial position of the diffusion path (ΔE_i). When the initial position is Oct, ΔE_i is set to zero. The actual diffusion barrier ΔE_t is then $\Delta E_i + \Delta E_{NEB}$. Even though the NEB calculations show that the Bc-Hex and the C-Hex paths have relatively small energy barriers (0.46 and 0.73 eV, respectively), the actual activation energies of diffusion (ΔE_t) are approximately 2.1 eV if the energy penalties for the initial sites are taken into account. Consistent with the earlier calculations of the static energy barrier (ΔE_s), the NEB simulations confirm that the Oct-C-Oct transition has the smallest diffusion energy barrier (1.39 eV).

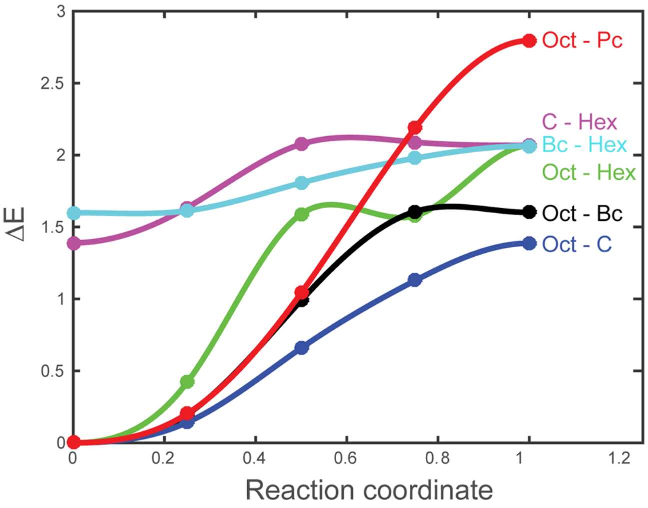

Figure 2. Activation energies of a single B atom along different diffusion trajectories calculated by the NEB method. The energy profile at the starting point takes into account the probability of B being filled at the initial position of the each path.

Table 2. Activation Energies Calculated by the NEB Method for a Single B Atom along Various Diffusion Trajectories

diffusion paths	ΔE_{NEB} (eV)	ΔE_{i} (eV)	ΔE_{t} (eV)
Oct-C	1.39	0	1.39
Oct-Bc	1.64	0	1.64
Oct-Hex	2.07	0	2.07
Oct-Pc	2.80	0	2.8
Bc-Hex	0.46	1.6	2.06
C-Hex	0.73	1.39	2.12

The Oct-Bc-Oct transition is the next preferred path with an energy barrier of 1.64 eV. Although the difference in the energy barrier between the two favorable paths is not large (0.25 eV), the corresponding Boltzmann factor, $\exp(-0.25/k_BT)$, where k_B is the Boltzmann constant and T is the temperature, indicates that diffusion along the second favorable path is approximately 18 times less likely than along the first path at 1000 K, the temperature where the intermixing between B and Zr actively occurs.[12] Other transition paths do not contribute to the diffusion kinetics much as they have higher energy barriers. It is clear that B transport in crystalline Zr is highly anisotropic and that the hopping step from the octahedral to the crowdion site in the basal planes dominates the diffusion kinetics of B in Zr.

We next examine the energetics, structural features, and diffusion kinetics in the intermediate compounds ZrB_x, $0.25 \leq x \leq 2$. We incrementally increase the B concentration in the Zr host. At each B concentration, we perform a Delaunay triangulation analysis to identify the largest void size in the lattice to accommodate insertion of B. Those void spaces are generally regarded as energetically favorable for B insertion.[25] In crystalline Zr, the centers of the largest voids correspond to the octahedral sites. B insertion drastically disorders the Zr lattice. We show in Figure 3a four representative structures, $\mathrm{ZrB}_{0.5}$, ZrB, $\mathrm{ZrB}_{1.5}$, and ZrB_2. More details of the structural evolution upon B insertion can be found in Figure S1. For each configuration, we calculate the enthalpy of formation from $E_f = [E_{m\mathrm{Zr}-n\mathrm{B}} - mE_{\mathrm{Zr}} - nE_{\mathrm{B}}]/(m + n)$, where m and n represent the number of Zr and B atoms, respectively. The dependence of E_f on the composition is plotted in Figure 3b. Note that the Oct site, the only stable site with a negative value of the formation energy shown in Table 1, has an equivalent number of Zr host atoms. Therefore, the ZrB phase represents the case where all Oct sites are filled by B. This structure has the lowest enthalpy

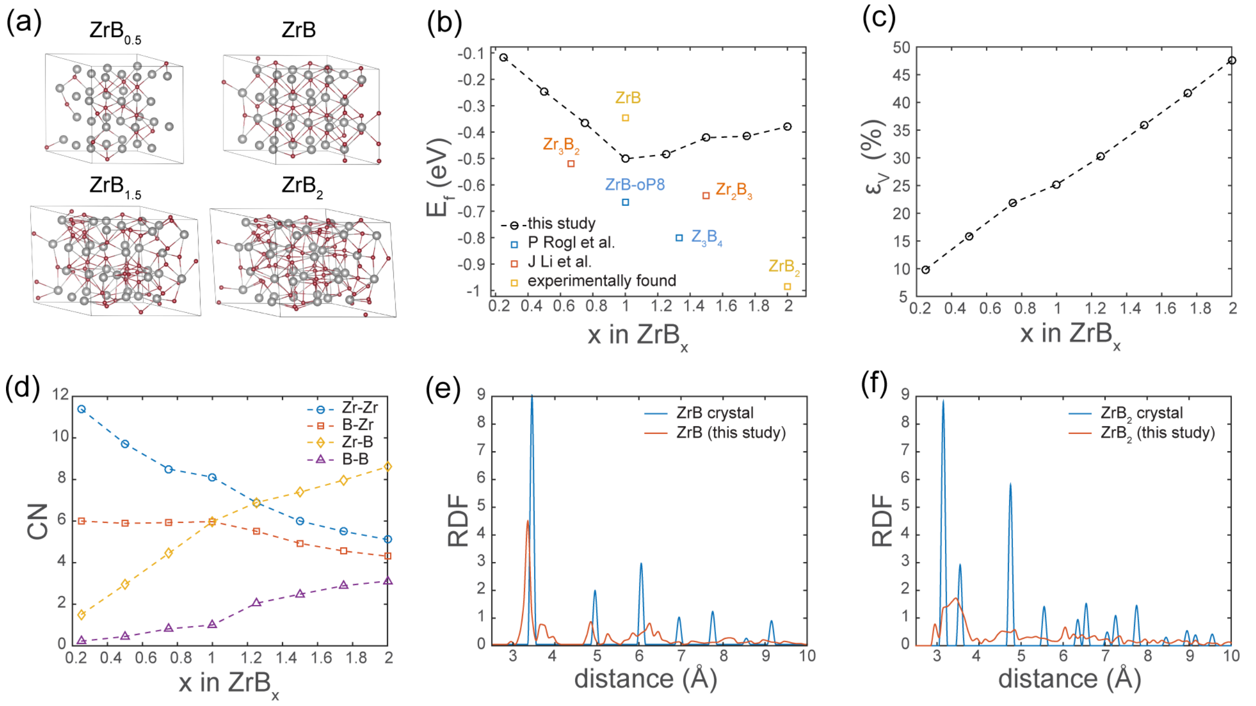

Figure 3. Structural and energetic features of $\mathrm{ZrB}_{0.25\leq x\leq 2}$. (a) Representative geometries of the ZrB_x structures. (b) Enthalpy of formation of ZrB_x in this work (circles) and the values of crystalline references (squares). (c) Volumetric strain (d) Coordination numbers of Zr−Zr, B−Zr, Zr−B, and B−B pairs in the ZrB_x structures. (e, f) RDF of ZrB and ZrB_2 for the Zr−Zr pairs. RDFs of crystalline references are included for comparison (blue).

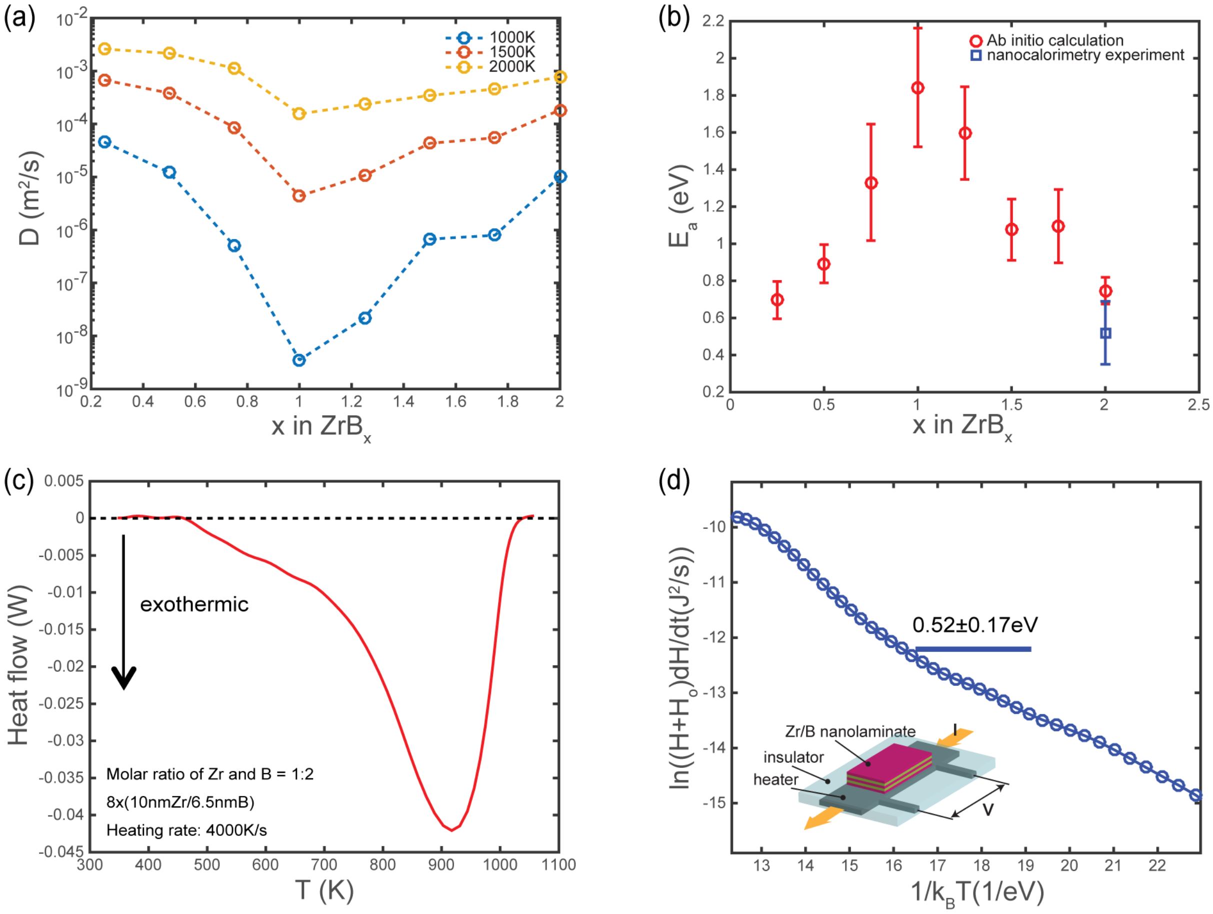

Figure 4. AIMD simulations and nanocalorimetry measurement to quantify the diffusion kinetics in ZrB_x. (a) B diffusivity vs composition at different temperatures of 1000, 1500, and 2000 K obtained from the MD simulations. (b) Red circles show the activation energies of B diffusion calculated from MD simulations. The error bars are calculated by linear fitting the MSD in different time ranges as detailed in Figure S2. Blue squares represent the experimental value by nanocalorimetry measurements. (c) Heat flow as a function of temperature obtained from a nanocalorimetry measurement on a Zr/B nanolaminate with a bilayer period of 16.5 nm. (d) A plot to obtain the activation energy of the diffusion in the Zr/B nanolaminate. The schematic of the nanocalorimetry sensor is depicted in the inset.

of formation and is the most energetically favorable among the metastable compounds. We also include for comparison reference data points that correspond to experimentally found or theoretically predicted Zr−B crystalline phases.[22,26] As expected, most of the crystalline phases have a smaller E_f compared to the metastable structures at the same concentration. One exception is that the ZrB phase in this study has a smaller E_f than the rock-salt phase reported in experiments. Figure 3c shows the evolution of the volumetric strain as a function of the B concentration. The slope of the volumetric strain remains very nearly constant throughout the entire range. We fit the dependence of the volumetric strain on the B concentration using a linear function and obtain the partial molar volume of B in Zr, $\Omega_{B-Zr} = 0.51 \times 10^{-29}$ m^3. The large volumetric deformation during Zr−B alloying is accommodated by the amorphization of the Zr lattice and the gradual rearrangement of the structure through Zr−Zr bond breaking and Zr−B cluster formation. To examine the bonding mechanism, we measure the evolution of the atomic coordination at various concentrations. A physically meaningful measure of atomic coordination is needed to define the atomic bonds. We define Zr−Zr atoms to be bonded if their distance is within 10% of the Zr−Zr bond length in bulk crystalline ZrB_2, which corresponds to a largest bond distance of 3.50 Å. Likewise, we define that a Zr atom is bonded with a B atom if their distance is smaller than 2.81 Å and that two B atoms are bonded to each other if their bond length is <2.02 Å. Figure 3d shows the average values of the coordination numbers. The Zr−Zr coordination steadily decreases, indicating a constant breaking of the bonds between the host atoms. Interestingly, the rates of bond breaking and formation change discontinuously at the ZrB composition, indicative of the more drastic structural change that occurs beyond this composition. More specifically, the CN for the B−Zr pairs stays nearly 6 for $ZrB_{x\leq 1}$, which is the same as the CN for the Oct site (Table 1). When the B concentration increases, the CN starts to decrease, indicating that metastable sites are now being filled. We find that most of the additional B atoms in $ZrB_{x>1}$ occupy Hex-like sites, which facilitates amorphization of the structure. This feature is also evident in the plot of the radial distribution function (RDF) for the Zr−Zr pairs; the structure remains largely crystalline up to the composition of ZrB (Figure 3e), but amorphization proceeds quickly beyond this point (Figure 3f).

We then quantify the diffusivity of B in various Zr−B compounds. We perform ab initio molecular dynamics (AIMD) simulations based on DFT using the eight relaxed structures with different B concentrations ($ZrB_{0.25\leq x\leq 2}$). Molecular dynamics (MD) calculations are carried out at temperatures of 1500, 1625, 1750, 1875, 2000, and 2500 K. The supercells are allowed to dynamically equilibrate at each temperature for

10,000 time steps; each step corresponding to 2 fs. We calculate the mean square displacement (MSD) of B using MSD = $\langle |r_i(t) - r_i(0)|^2\rangle$, where $r_i(t)$ is the position of atom i at time t, $r_i(0)$is the position of atom i in the initial configuration, and $\langle\cdot\rangle$ represents an average over the ensemble of atoms. The calculated MSD of B in eight zirconium borides is shown in Figure S2. Here we only consider the MSDs of B because B are much more mobile in the mixing process compared to Zr. The diffusivity of B can be derived from the MSD using Einstein's relationship, $D = \lim_{t\to\infty}(1/6t)\langle|r_i(t) - r_i(0)|^2\rangle$. We calculate the diffusivity of B at different temperatures and fit the data using the standard expression for diffusivity, $D = D_0 \exp(-E_a/k_BT)$, where E_a is the energy barrier. Logarithmic plots of the B diffusivity versus 1000/T are shown in Figure S2 for eight representative compositions. Figure 4a shows the B diffusivity for each concentration at temperatures of 1000, 1500, and 2000 K. For all temperatures, the diffusivity is minimum at ZrB. The B concentration effect is striking at the lowest temperature (1000 K), with a difference of 4 orders of magnitude between the largest value for $ZrB_{0.25}$ and the smallest for ZrB. This is a consequence of the large activation energy for diffusion in the ZrB structure (Figure 4b); B fills all Oct sites in the structure making B transport through the structure very difficult. Effective transport of B would probably require a vacancy mechanism in this case.

Nanocalorimetry experiments using a special sensor (Figure 4d inset) have been performed on a Zr/B reactive nanolaminate with a bilayer period of 16.5 nm and a specific atomic ratio of Zr:2B. The results are shown in Figure 4c,d. The principle of the nanocalorimetry technique is reported in our previous work,[11,27,28] and experimental details are included in the methodology section. Zr/B reactive nanolaminates are of technological interest as a means of synthesizing highly textured ZrB_2 coatings at relatively low temperatures.[12] As illustrated in Figure 4c, the exothermic reaction starts at 470 K and is completed at 1050 K, peaking around 910 K. The exothermic reaction in this temperature range is caused by the interdiffusion of B and Zr, yielding an amorphous Zr−B alloy.[12] The peak temperature observed here is higher than previous nanocalorimetry measurements[12] on Zr/B nanolaminates with smaller bilayer periods because of the increased diffusion distance in these nanolaminates.

With the formation of amorphous structures observed in both the Zr/B nanolaminate sample and in the AIMD simulations, it is possible to directly compare the results to cross validate experiments and simulations. Figure 4d shows a graph of $\ln[(H + H_o)\mathrm{d}H/\mathrm{d}t]$ versus $1/k_BT$ for the temperature range of 500−930 K, where H is the enthalpy released during the exothermic reaction and H_0 is the enthalpy that corresponds to the mixed Zr/B interface layers (1.5 nm, approximately)[12] formed during the nanolaminate deposition process. The slope of this curve has been shown to be the diffusion activation energy for a number of multilayered nanolaminate systems.[12,29,30] The graph is nearly linear with a slope of 0.52 eV, a value that is marked in Figure 4b and that agrees well with the AIMD simulations for the same concentration.

In conclusion, we have studied the thermodynamics and kinetics of the solid-state alloying process of Zr−B for the synthesis of ZrB_2. In the limit of low B concentration, B transport in crystalline Zr is highly anisotropic and is dominated by the Oct-C transition between the Zr basal planes. With increasing B concentration, the Zr structure is gradually amorphized as a result of the rupture of host atom bonds and the formation of Zr−B clusters. The ZrB phase maintains the lowest enthalpy of formation among all the metastable compounds. The ZrB energy landscape has the highest energy barrier for B transport, yielding the lowest B diffusivity, consistent with the results obtained in the MD simulations. Nanocalorimetry measurements on Zr/B reactive nanolaminates allow experimental determination of the diffusion energy barrier and are in good agreement with the atomistic simulations for ZrB_2. The fundamental understanding of the Zr and B interdiffusion process arising from the combination of atomistic modeling and experimentation provides valuable insight that can be used to optimize the fabrication of ZrB_2 coatings for a range of practical applications.

Methods. The first-principles calculations based on the DFT are carried out using the Vienna ab initio simulation package (VASP).[31] The projected-augmented-waves (PAW)[32] with the Perdew−Burke−Ernzerhof (PBE)[33] exchange−correlation potentials are adopted. For Zr and B, $4s^24p^65s^24d^2$ and $2s^22p$ valence states are treated, respectively. The cutoff energy for plane waves is set to 400 eV, and the forces are converged to within 0.02 eV/Å. We use a 54-atom Zr supercell (3 × 3 × 3) and one B atom for the simulations to identify the interstitial sites and for the NEB[34,35] calculations. For the relaxations of the eight structures with different B concentrations ($ZrB_{0.25\le x\le 2}$) and for the AIMD simulations, supercells with 36 Zr atoms (3 × 3 × 2) and the number of B atoms corresponding to each concentration are utilized. For Brillouin zone sampling, 6 × 6 × 4, 3 × 3 × 2, 3 × 3 × 3, and 1 × 1 × 1 k-point meshes in the Monkhorst−Pack scheme are employed for the simulations of the interstitial sites, the NEB calculations, the relaxations of the $ZrB_{0.25\le x\le 2}$ structures, and the AIMD simulations, respectively.

Nanocalorimetry sensors are fabricated using conventional Si-based microfabrication techniques. Details of sensor fabrication and working principle can be found elsewhere.[12,27,28] A nanolaminate with alternating Zr and B layers (molar ratio = 1:2, bilayer period = 16.5 nm, total thickness = 82.5 nm) is magnetron sputter deposited using 99.99% Zr and 99.95% B targets inside a chamber with a base pressure better than 2×10^{-7} Torr. A scanning nanocalorimetry measurement is performed in vacuum at a heating rate of 4000 K/s, during which both the power supplied to and the temperature of the calorimetry sensor are measured. The raw power and temperature data are utilized to determine the reactive heat flow of the nanolaminate sample following the procedure developed in our previous work.[11]

■ ASSOCIATED CONTENT

Supporting Information

The Supporting Information is available free of charge on the ACS Publications website at DOI: 10.1021/acs.nanolett.5b02260.

Structures, MSDs, and diffusivities of Zr−B alloys (PDF)

■ AUTHOR INFORMATION

Corresponding Authors

*E-mail: kjzhao@purdue.edu.
*E-mail: vlassak@seas.harvard.edu.

Notes

The authors declare no competing financial interest.

■ ACKNOWLEDGMENTS

This work was supported by the Air Force Office of Scientific Research under grant no. FA9550-12-1-0098. It was performed in part at the Center for Nanoscale Systems at Harvard University, which is supported by the National Science Foundation under award no. ECS-0335765, and at the Materials Research Science and Engineering Center at Harvard University, which is supported by the National Science Foundation under award no. DMR-14-20570. K.Z. is grateful for the start-up funding provided by Purdue University and for the Haythornthwaite Foundation Initiation Grant from the American Society of Mechanical Engineering.

■ REFERENCES

(1) Fahrenholtz, W. G.; Hilmas, G. E.; Talmy, I. G.; Zaykoski, J. A. *J. Am. Ceram. Soc.* **2007**, *90* (5), 1347−1364.
(2) Opeka, M. M.; Talmy, I. G.; Zaykoski, J. A. *J. Mater. Sci.* **2004**, *39* (19), 5887−5904.
(3) Upadhya, K.; Yang, J. M.; Hoffman, W. P. *Am. Ceram Soc. Bull.* **1997**, *76* (12), 51−56.
(4) Carenco, S.; Portehault, D.; Boissiere, C.; Mezailles, N.; Sanchez, C. *Chem. Rev.* **2013**, *113* (10), 7981−8065.
(5) Liu, R.; Bell, A.; Ponce, F. A.; Kamiyama, S.; Amano, H.; Akasaki, I. *Appl. Phys. Lett.* **2002**, *81* (17), 3182−3184.
(6) Suda, J.; Matsunami, H. *J. Cryst. Growth* **2002**, *237*, 1114−1117.
(7) Tolle, J.; Roucka, R.; Tsong, I. S. T.; Ritter, C.; Crozier, P. A.; Chizmeshya, A. V. G.; Kouvetakis, J. *Appl. Phys. Lett.* **2003**, *82* (15), 2398−2400.
(8) Yamada-Takamura, Y.; Wang, Z. T.; Fujikawa, Y.; Sakurai, T.; Xue, Q. K.; Tolle, J.; Liu, P. L.; Chizmeshya, A. V. G.; Kouvetakis, J.; Tsong, I. S. T. *Phys. Rev. Lett.* **2005**, *95* (26), 266105.
(9) Hu, C. W.; Chizmeshya, A. V. G.; Tolle, J.; Kouvetakis, J.; Tsong, I. S. T. *J. Cryst. Growth* **2004**, *267* (3−4), 554−563.
(10) Roucka, R.; D'Costa, V. R.; An, Y. J.; Canonico, M.; Kouvetakis, J.; Menendez, J.; Chizmeshya, A. V. G. *Chem. Mater.* **2008**, *20* (4), 1431−1442.
(11) Lee, D.; Sim, G. D.; Xiao, K. C.; Choi, Y. S.; Vlassak, J. J. *J. Appl. Phys.* **2013**, *114* (21), 214902.
(12) Lee, D.; Sim, G. D.; Xiao, K. C.; Vlassak, J. J. *J. Phys. Chem. C* **2014**, *118* (36), 21192−21198.
(13) Samsonov, G.; Zhunkovskii, G. *Sov. Powder Metall. Met. Ceram.* **1970**, *9* (6), 472−478.
(14) Willaime, F. *J. Nucl. Mater.* **2003**, *323* (2−3), 205−212.
(15) Mendelev, M. I.; Bokstein, B. S. *Philos. Mag.* **2010**, *90* (5), 637−654.
(16) Samolyuk, G. D.; Barashev, A. V.; Golubov, S. I.; Osetsky, Y. N.; Stoller, R. E. *Acta Mater.* **2014**, *78*, 173−180.
(17) Vajeeston, P.; Ravindran, P.; Ravi, C.; Asokamani, R. *Phys. Rev. B* **2001**, *63* (4), 045115.
(18) Kumar, R.; Mishra, M. C.; Sharma, B. K.; Sharma, V.; Lowther, J. E.; Vyas, V.; Sharma, G. *Comput. Mater. Sci.* **2012**, *61*, 150−157.
(19) Middleburgh, S. C.; Parfitt, D. C.; Blair, P. R.; Grimes, R. W. *J. Am. Ceram. Soc.* **2011**, *94* (7), 2225−2229.
(20) Lawson, J. W.; Bauschlicher, C. W.; Daw, M. S. *J. Am. Ceram. Soc.* **2011**, *94* (10), 3494−3499.
(21) Li, H.; Zhang, L. T.; Zeng, Q. F.; Wang, J. J.; Cheng, L. F.; Ren, H. T.; Guan, K. *Comput. Mater. Sci.* **2010**, *49* (4), 814−819.
(22) Li, J.; Fan, C. *Phys. Chem. Chem. Phys.* **2015**, *17* (2), 1180−1188.
(23) Hennig, R. G.; Trinkle, D. R.; Bouchet, J.; Srinivasan, S. G.; Albers, R. C.; Wilkins, J. W. *Nat. Mater.* **2005**, *4* (2), 129−133.
(24) Wu, H. H.; Trinkle, D. R. *Phys. Rev. Lett.* 2011, *107*, (4), 045504.
(25) Zhang, Y. F.; Li, Y. J.; Wang, Z. Y.; Zhao, K. J. *Nano Lett.* **2014**, *14* (12), 7161−7170.
(26) Rogl, P.; Potter, P. E. *CALPHAD: Comput. Coupling Phase Diagrams Thermochem.* **1988**, *12* (2), 191−204.
(27) McCluskey, P. J.; Vlassak, J. J. *J. Mater. Res.* **2010**, *25* (11), 2086−2100.
(28) McCluskey, P. J.; Vlassak, J. J. *Thin Solid Films* **2010**, *518* (23), 7093−7106.
(29) Highmore, R. J.; Evetts, J. E.; Greer, A. L.; Somekh, R. E. *Appl. Phys. Lett.* **1987**, *50* (10), 566−568.
(30) Highmore, R. J.; Somekh, R. E.; Evetts, J. E.; Greer, A. L. *J. Less-Common Met.* **1988**, *140*, 353−360.
(31) Kresse, G.; Furthmuller, J. *Phys. Rev. B: Condens. Matter Mater. Phys.* **1996**, *54* (16), 11169−11186.
(32) Kresse, G.; Joubert, D. *Phys. Rev. B: Condens. Matter Mater. Phys.* **1999**, *59* (3), 1758−1775.
(33) Perdew, J. P.; Burke, K.; Ernzerhof, M. *Phys. Rev. Lett.* **1996**, *77* (18), 3865−3868.
(34) Henkelman, G.; Jonsson, H. *J. Chem. Phys.* **2000**, *113* (22), 9978−9985.
(35) Henkelman, G.; Uberuaga, B. P.; Jonsson, H. *J. Chem. Phys.* **2000**, *113* (22), 9901−9904.

DOI: 10.1021/acs.nanolett.5b02260
Nano Lett. 2015, 15, 6553−6558